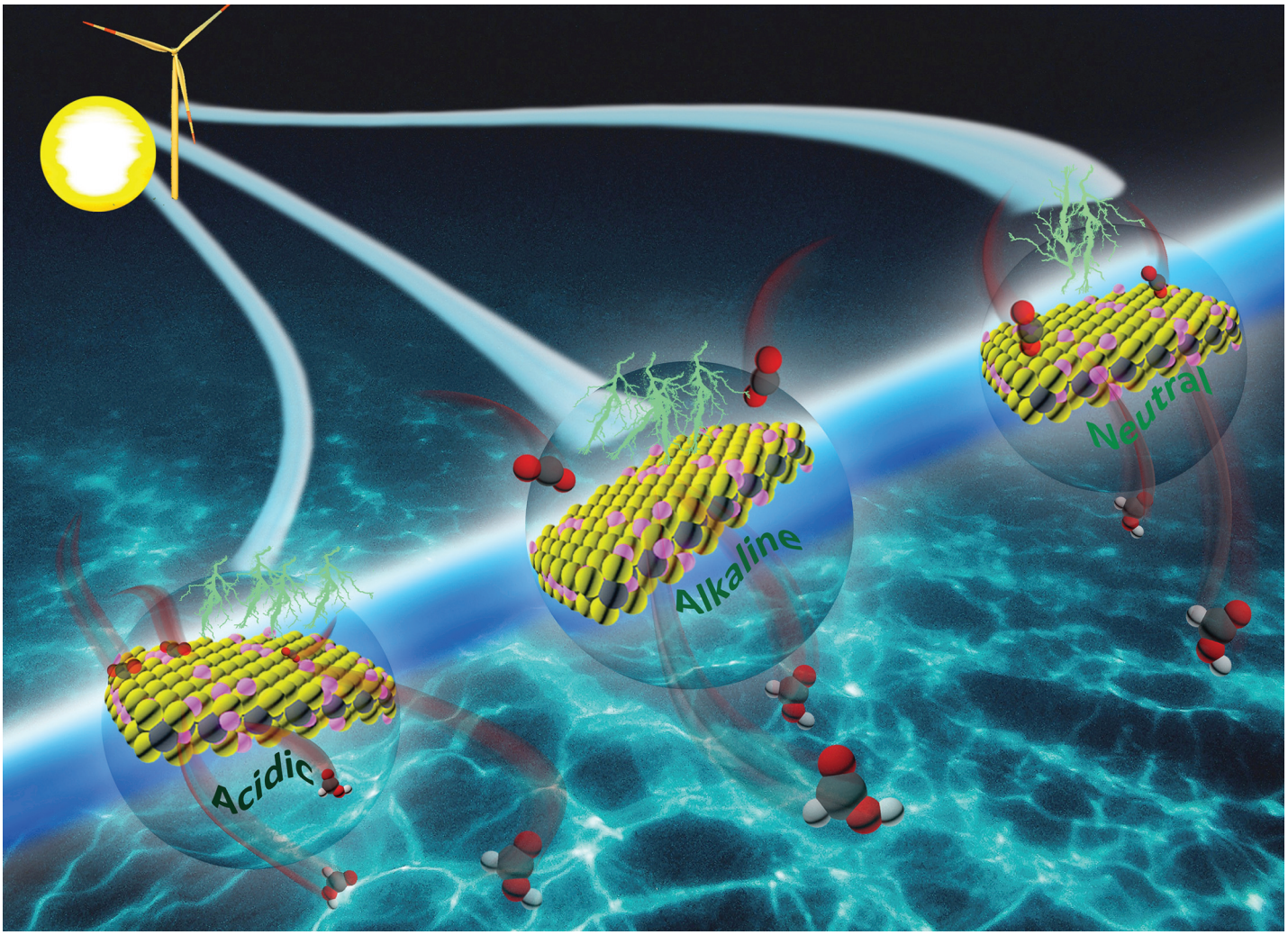

Showcasing research from State Key Laboratory of Clean and Efficient Coal Utilization, Taiyuan University of Technology.

Regulating the hydrophobic microenvironment of SnS_2 to facilitate the interfacial CO_2/H_2O ratio towards pH-universal electrocatalytic CO_2 reduction

This strategy empowers SnS_2-based catalysts to efficiently carry out the electrocatalytic CO_2 reduction reaction across the entire pH range. Moreover, the modified catalysts demonstrated an ultra-high single-pass CO_2 conversion in an acidic electrolyte.

Image reproduced by permission of Wen-Ying Li from *Green Chem.*, 2025, **27**, 5498.

As featured in:

See Yaling Jia, Wen-Ying Li *et al.*, *Green Chem.*, 2025, **27**, 5498.

ROYAL SOCIETY OF CHEMISTRY

rsc.li/greenchem

Registered charity number: 207890

Green Chemistry

PAPER

View Article Online
View Journal | View Issue

Cite this: *Green Chem.*, 2025, **27**, 5498

Regulating the hydrophobic microenvironment of SnS_2 to facilitate the interfacial CO_2/H_2O ratio towards pH-universal electrocatalytic CO_2 reduction†

Zhiwei Dong, [a] Yaling Jia, *[a] Zeyu Wang, [a] Antony Rajendran [b] and Wen-Ying Li *[a]

Received 6th February 2025,
Accepted 28th March 2025

DOI: 10.1039/d5gc00635j

rsc.li/greenchem

Electrocatalytic CO_2 reduction to formic acid is a promising strategy to obtain value-added chemicals and achieve the carbon cycle. However, its practical application is generally impeded by the limited accessibility of CO_2 to the catalyst's surface and the lack of an efficient universal catalyst across different pH levels. Herein, we report a new catalyst, *i.e.*, SnS_2 decorated with a hydrophobic polymer polyvinylidene fluoride (SnS_2 + PVDF), for the effective electrocatalytic CO_2 reduction to formate/formic acid across a wide pH range in a flow cell. This catalytic system accomplishes a remarkable faradaic efficiency for the formic acid production in alkaline (98%), neutral (86%), and acidic (93%) electrolytes. Also, the single-pass carbon efficiency reaches up to 72.77% in acidic electrolytes. Water contact angle measurements in association with *in situ* attenuated total reflectance surface-enhanced infrared absorption spectroscopy results indicate that the inclusion of PVDF creates a hydrophobic microenvironment which increases the CO_2/H_2O ratio near the surface of SnS_2 particles. As a consequence, SnS_2 particles enjoy the enhanced CO_2 concentration around their surface to form many three-phase (solid–liquid–gas) boundaries. *In situ* Raman spectra combined with electrocatalytic studies reveal that SnS_2 undergoes reconstitution to form catalytically active Sn/SnS_2 during the reaction. These findings ensure and expand the generality of a hydrophobic microenvironment regulation strategy in promoting electrocatalytic CO_2 reduction to formic acid.

Green foundation

1. The electrocatalytic conversion of CO_2 into formic acid presents an appealing means for generating valuable chemicals using renewable energy while contributing to the carbon cycle, which is of vital significance for alleviating energy and environmental challenges.
2. This study reports that the SnS_2 + PVDF 50 electrode elevates the local CO_2/H_2O ratio on the catalyst surface and constructs more gas–electrolyte–liquid triple-phase boundaries. The catalyst exhibits excellent performance across a wide range of pH for electrocatalytic CO_2 reduction to formate/formic acid. This enhances the reaction's practicability in diverse environmental settings, further contributing to the global effort to reduce carbon emissions.
3. The in-depth investigation of the optimal CO_2/H_2O ratio in different catalytic systems and the specific catalyst-reconstitution mechanism during electrochemical CO_2 reduction need further exploration in the future.

Introduction

The continuous increase of atmospheric CO_2 concentration due to fossil fuel combustion, deforestation, and industrial activities has led to severe environmental impact.[1–3] The electrocatalytic CO_2 reduction reaction (ECO_2RR) using renewable energy offers a potential pathway to mitigate CO_2 concentration by converting CO_2 into value-added fuels and chemicals.[4–6] Among the produced value-added fuels, formic acid has drawn considerable attention due to its wide applications as an organic chemical intermediate and a hydrogen storage carrier.[7] Notably, Sn-based catalysts have emerged as promising candidates for selective formic acid production due to their optimal adsorption strength for the key *OCOH intermediate. Besides, Sn is a low-toxic and naturally abundant metal. These inherent characteristics in addition to their

[a]*State Key Laboratory of Clean and Efficient Coal Utilization, Taiyuan University of Technology, Taiyuan 030024, China. E-mail: jiayaling@tyut.edu.cn, ying@tyut.edu.cn; Tel: +86 351 6018453; Fax: +86 351 6018453*
[b]*Department of Chemistry, Mepco Schlenk Engineering College (Autonomous), Sivakasi-626005, Tamil Nadu, India. E-mail: anto.chemist@gmail.com*
† Electronic supplementary information (ESI) available. See DOI: https://doi.org/10.1039/d5gc00635j

unique electronic configuration underline Sn-based materials as promising candidates for the ECO_2RR.[8–10] However, the phenomenon of 'water flooding' results in insufficient interfacial CO_2 on the catalyst surface in the flow cell during the ECO_2RR, which in turn favors the hydrogen evolution reaction (HER).[11–14] Hence, developing a strategy to optimize the CO_2/H_2O ratio on the catalyst surface is a prerequisite for the successful ECO_2RR.

Recently, regulating the hydrophobic microenvironment has been proven to be effective in enriching CO_2 concentration on the catalyst surface during the ECO_2RR.[15–17] This strategy significantly enhances the selectivity of C_1 and C_{2+} products by controlling the local CO_2/H_2O ratio and suppressing the competing HER. For instance, Zheng *et al*. modified the Cu electrode using quaternary ammonium functionalized polynorbornene ionomers and confirmed that the strong hydrophobicity extended the residence of the *CO intermediate on Cu surfaces, thus improving the rate of C–C coupling and boosting the selectivity of C_{2+} products. Similarly, a thin polymer coating has been used to modulate the ratio of CO_2/H_2O on the Cu surface, which could improve the selectivity of C_{2+} products and offer considerable energy efficiency at nearly industrialized current densities.[18] Qiu *et al.* constructed a special CO_2-philic and hydrophobic interface by employing a defective carbon to modify a Bi nanoparticle catalyst.[19] This catalyst with a stable spatial structure accelerated the mass transfer of CO_2 and inhibited the competitive HER, significantly improving the selectivity of formate. Wang *et al.* further demonstrated the effectiveness of this strategy by decorating an In_2O_3 electrode with fluoropolymers, which increased the local CO_2 concentration near the catalyst surface and boosted the production of formate.[17] Few reports are available in the literature on regulating the hydrophobic microenvironment of Cu, Bi, and In-based catalysts. However, such reports on Sn-based catalysts are very rare and are not reported so far to the best of our knowledge. In this context, utilizing a hydrophobic polymer to enhance the ECO_2RR performance and uncover the underlying mechanisms seems crucial for preparing high-performance Sn-based ECO_2RR catalysts.

The ECO_2RR in alkaline and neutral electrolytes has been proven to be an effective method to alleviate the competing HER. However, it inevitably leads to the formation of carbonates or bicarbonates that diminish the electrolyte's conductivity and the efficiency of CO_2 utilization.[20–22] Employing an acidic electrolyte seems an excellent idea to solve this issue but the acidic electrolytes promote the competitive HER and thus hinder the effective CO_2 conversion.[23–25] Therefore, the pH-universal ECO_2RR has gained interest in picking an appropriate reaction environment according to practical demand. Also, the ability to operate across a wide pH range enhances the technology's applicability in diverse environmental settings.[26,27] So, developing an efficient ECO_2RR catalyst to form formic acid across a full pH range is of greater importance.

Based on the above facts, in this work, we have decorated SnS_2 nanoflowers with a hydrophobic polymer (polyvinylidene fluoride, PVDF) using a facile method. The obtained electrode SnS_2 + PVDF 50 displays an excellent performance: 98% formate faradaic efficiency (FE) at −0.8 V *vs.* reversible hydrogen electrode (RHE) (all the potentials are referred to RHE in this work) in 1 M KOH, 93% HCOOH FE at −1.9 V in 0.05 M H_2SO_4 + 0.5 M K_2SO_4 and 86% formate FE at −1.2 V in 0.5 M $KHCO_3$. It is important to note that the SnS_2 + PVDF 50 electrode exhibits robust stability (>30 h) in the alkaline electrolyte under a current density of 150 mA cm^{-2}. *In situ* attenuated total reflectance surface-enhanced infrared absorption spectroscopy (ATR-SEIRAS) reveals that the introduction of PVDF increases the local ratio of CO_2/H_2O near the surface of SnS_2 and thus enhances the accessibility of CO_2 to the catalyst while suppressing the HER. Furthermore, *in situ* Raman studies along with electrocatalytic studies indicate the reconstruction of SnS_2 to the Sn/SnS_2 composite (the real catalytically active phase).

Results and discussion

Characterization of SnS_2

SnS_2 nanoflowers were synthesized using a hydrothermal method.[28] The powder X-ray diffraction (XRD) pattern (Fig. 1a) supports the successful preparation of SnS_2 in line with JCPDS No. 83–1705. As shown in the scanning electron microscopy (SEM) image (Fig. 1b), the prepared SnS_2 particles exhibit a nanoflower morphology. X-ray photoelectron spectroscopy (XPS) and Raman spectra of SnS_2 on carbon paper (CP) further confirm the formation of SnS_2 (Fig. S1 of the ESI†). SnS_2 was modified using a hydrophobic polymer (PVDF) and a hydrophilic polymer (polyvinyl pyrrolidone, PVP).[29] As indicated by the XRD pattern (Fig. 1a), the crystal structure of the SnS_2 + PVP electrode remains unchanged as compared to that of the pure SnS_2 electrode. For SnS_2 + PVDF 50, an additional diffraction peak appears at 20.2° due to the (110) plane of PVDF.[30]

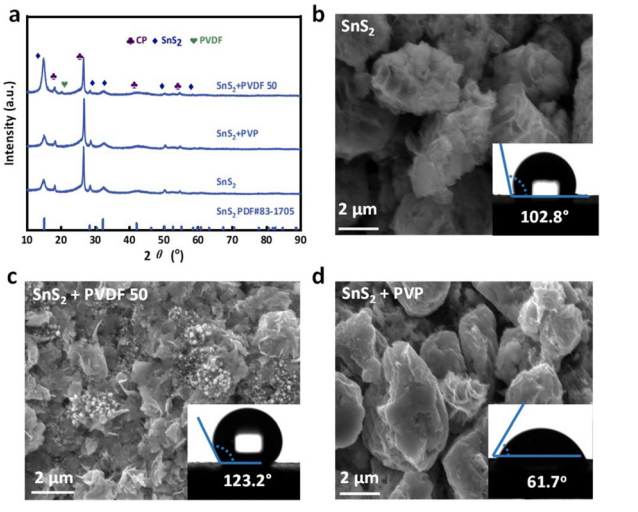

Fig. 1 Physical characterization of the as-synthesized catalysts. (a) XRD patterns. The SEM images and water contact angles of (b) SnS_2 + PVDF 50, (c) SnS_2, and (d) SnS_2 + PVP.

PVDF particles cover the surface of the SnS_2 layer in the SnS_2 + PVDF electrode (Fig. 1c). This type of coverage is not observed in the SnS_2 + PVP electrode (Fig. 1d) except in a block-shaped morphology. Furthermore, the introduction of PVDF and PVP is confirmed by XPS. In the XPS spectrum of the SnS_2 + PVDF electrode, the peak at 688.97 eV for the F 1*s* high-resolution spectrum and the peaks at 290.88 and 286.09 eV for high-resolution C 1*s* spectrum are characteristic peaks of fluorinated hydrocarbons (Fig. S2†).[31] In the XPS spectrum of the SnS_2 + PVP electrode, the strong N 1*s* peak at 400.11 eV is ascribed to PVP (Fig. S3†).[32] These results indicate the incorporation of PVDF and PVP into the SnS_2 electrode. To investigate the impact of polymer modification on the hydrophobicity of SnS_2, the water contact angle measurement was conducted. As illustrated in (Fig. 1b, c, and d), water contact angles for SnS_2 + PVDF 50, SnS_2, and SnS_2 + PVP were 123.2°, 102.8°, and 61.7°, respectively. This underlines that PVDF enhances the hydrophobicity of the SnS_2 electrode, while PVP enhances its hydrophilicity.

ECO_2RR performance

To elucidate the impact of various microenvironments on the electrocatalytic performance of SnS_2, we initially conducted ECO_2RR experiments in the flow cell (more details in Fig. S4†) in 1.0 M KOH.[33–35] Evaluation of the FE at varying potentials reveals that formate/formic acid is the sole liquid-phase product (Fig. S5†). To assess the activity of three distinct electrodes during the ECO_2RR (SnS_2, SnS_2 + PVDF 50, and SnS_2 + PVP), linear sweep voltammetry (LSV) curves were initially recorded. As shown in Fig. S6,† the SnS_2 + PVDF 50 electrode exhibits a significantly enhanced current density along with a more positive onset potential compared to both pure SnS_2 and SnS_2 + PVP electrodes. This emphasizes its superior activity for the ECO_2RR. The standard curve for calculating formate FE is shown in Fig. S7.† According to Fig. 2a, the SnS_2 + PVDF 50 electrode demonstrates a high FE for formate across an extensive potential range from −0.8 V to −1.1 V (>90%).

Compared to both SnS_2 and SnS_2 + PVP, the SnS_2 + PVDF 50 electrode displays the highest formate FE and the highest formate production rate in 1 M KOH (Fig. S8†). Conversely, the SnS_2 + PVP electrode exhibits the highest H_2 FE. To find out the impact of the SnS_2/PVDF ratio on the ECO_2RR performance, a few SnS_2 + PVDF electrodes varying in the quantity of PVDF were prepared. As illustrated in Fig. S9,† the SnS_2 + PVDF 50 electrode exhibits optimal activity and selectivity. Meanwhile, the single-pass carbon efficiency (SPCE) was also determined to evaluate the practical viability of the catalyst. As shown in Fig. S10,† when the CO_2 flow rates decrease from 15 to 5 sccm, SPCE reaches its peak value of 31.63% at −1.2 V. Next, the long-term stability of the SnS_2 + PVDF 50 electrode in 1 M KOH was examined. As depicted in Fig. 2b, the SnS_2 + PVDF 50 electrode is significantly durable over time. On average, formate FE remains above 80% for more than thirty hours at 150 mA cm^{-2} in 1 M KOH, ultimately yielding a 2.67 mol L^{-1} formate solution.

The performance of the ECO_2RR was also evaluated in a neutral electrolyte 0.5 M $KHCO_3$. According to the LSV curves, the SnS_2 + PVDF 50 electrode exhibits superior performance

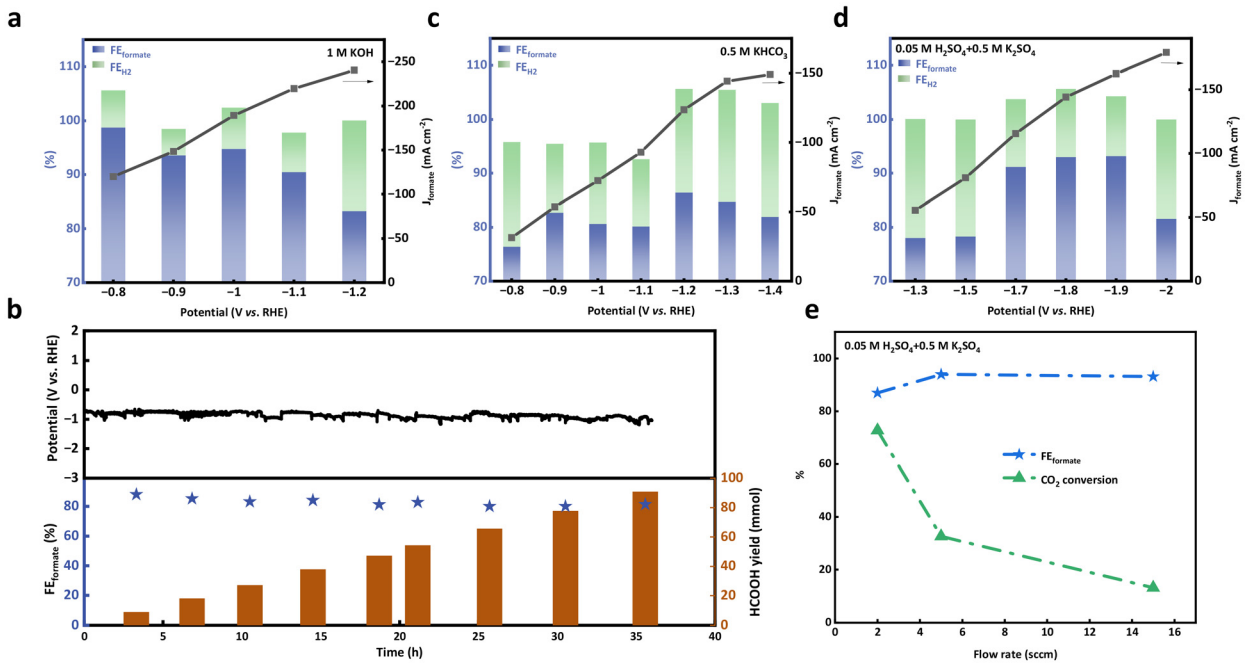

Fig. 2 ECO_2RR performance in a flow cell. The formate FE and formate partial current density of the SnS_2 + PVDF 50 electrode in (a) 1 M KOH, (c) 0.05 M H_2SO_4 + 0.5 M K_2SO_4, and (d) 0.5 M $KHCO_3$. (b) The ECO_2RR stability of the SnS_2 + PVDF 50 electrode under −150 mA cm^{-2} in 1 M KOH. (e) SPCE and formate FE comparison of the SnS_2 + PVDF 50 electrode under different CO_2 flow rates.

compared to both the SnS_2 and SnS_2 + PVP electrodes (Fig. S11†). Meanwhile, the SnS_2 + PVDF 50 electrode demonstrates a high formate FE over a broad potential range from −0.9 V to −1.4 V, exceeding 80% (Fig. 2c). Compared to the SnS_2 and SnS_2 + PVP electrodes in the 0.5 M $KHCO_3$ electrolyte, the SnS_2 + PVDF 50 electrode reaches the highest formate FE (Fig. S12a†). Furthermore, the SnS_2 + PVDF 50 electrode exhibits the highest rate of formate production at 1.8 mmol mg^{-1} h^{-1} along with an SPCE of 4.88% (Fig. S12c and d†).

To evaluate the pH-universal feasibility of the ECO_2RR, its performance was assessed in an acidic electrolyte (0.05 M H_2SO_4 + 0.5 M K_2SO_4). The SnS_2 + PVDF 50 electrode reveals a markedly improved current density and a more positive onset potential (Fig. S13†), along with a high FE for HCOOH across an extensive potential range from −0.8 V to −1.1 V (Fig. 2d). Meanwhile, the SnS_2 + PVDF 50 electrode achieves the highest HCOOH FE compared with SnS_2 and SnS_2 + PVP electrodes, as depicted in Fig. S14.† Also, the SnS_2 + PVDF 50 electrode attains an exceptional HCOOH production rate of 4.82 mmol mg^{-1} h^{-1}. As seen in Fig. 2e, SPCE reaches an optimal value of 72.77% at −1.9 V at a CO_2 flow rate of 2 sccm, which is better than some advanced catalysts (Table S1†). The SnS_2 + PVDF 50 electrode displays a superior performance invariably in alkaline, acidic, and neutral electrolytes compared with some advanced catalysts (Fig. S15, Tables S2 and 3†). Intriguingly, the SnS_2 + PVDF 50 electrode shows a better performance than a few advanced SnS_2-based catalysts (Table S4†).

Mechanism of performance enhancement

It is clear that the SnS_2 + PVDF 50 electrode significantly suppresses the HER while enhancing both the activity and selectivity of the CO_2RR. In contrast, the SnS_2 + PVP electrode severely inhibits both activity and selectivity in the ECO_2RR. To further elucidate the mechanism behind the impact of polymer modification on the catalyst performance of SnS_2 in the ECO_2RR, the electrochemically active surface area (ECSA) of the electrolytes was calculated. The ECSA is proportional to the electrochemical double-layer capacitance (C_{dl}) measured using CV curves (Fig. S16†).[36] The ECSA refers to the portion of an electrode that is wetted and accessible to the electrolyte.[15] It is hypothesized that the increased gas volume within the catalyst layer reduces its ECSA due to a decreased contact area with the electrolyte. As shown in Fig. 3a, the SnS_2 + PVDF 50 electrode exhibits an ECSA value of 0.86 mF cm^{-2}, which is lower than that of the unmodified electrode (0.96 mF cm^{-2}). The largest ECSA was recorded for the SnS_2 + PVP electrodes at 2.98 mF cm^{-2} while comparing with both SnS_2 and SnS_2 + PVDF 50 electrodes. This indicates that the increased likelihood of gas bubble formation around the SnS_2 + PVDF 50 electrode creates a more favorable environment for the production of formate during the CO_2RR. In contrast, the largest ECSA of the SnS_2 + PVP electrode contributes to the enhanced presence of electrolytes surrounding the SnS_2 + PVP electrode, which is more conducive to H_2 production.[15] Then, the electrochemical impedance spectroscopy (EIS) results for all three electrodes under the ECO_2RR conditions are shown in Fig. 3b. According

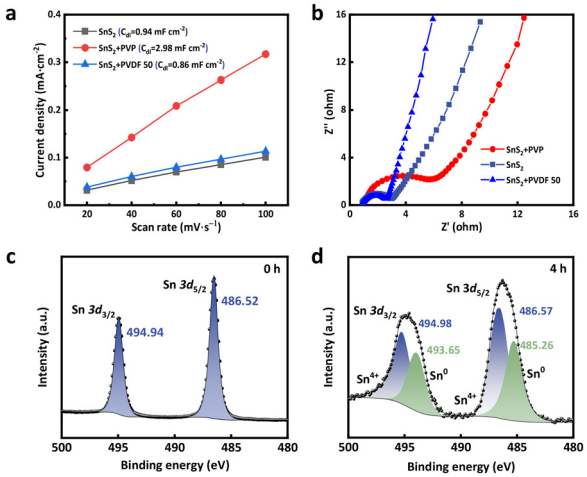

Fig. 3 (a) Linear relationship between the current density and scan rate for the SnS_2 + PVP, SnS_2, and SnS_2 + PVDF 50 electrodes for the estimation of ECSA. (b) EIS plots. The *in situ* reduction results of SnS_2 + PVDF 50 (c) Sn 3d XPS spectrum without electrolysis and (d) Sn 3d XPS spectrum after 4 h of electrolysis.

to the EIS results, the SnS_2 + PVDF 50 electrode exhibits the lowest charge transfer resistance (R_{ct}) while the SnS_2 + PVP electrode displays the highest R_{ct}. To quantitatively elucidate the dynamic evolution of Sn species in SnS_2 + PVDF 50 during the CO_2RR, CO_2 electrolysis was conducted at −1.2 V in a saturated 0.5 mol L^{-1} $KHCO_3$ solution. The results in Fig. S17a† reveal that SnS_2 gradually reduced to Sn which became the dominant phase after 30 min. A small amount of SnS_2 remained was observed even after 4 h of electrolysis. The corresponding results of electrolytic experiments carried out for different reaction time indicate the gradual increase of $FE_{formate}$ with the increase of electrolysis time (Fig. S17b†), suggesting that metallic Sn is the primary active phase. In the XPS spectra (Fig. 3c and d), the two characteristic peaks at 494.94 and 486.52 eV of the original Sn 3*d* spectrum are attributed to the predominate existence of the Sn^{4+} state.[37] After 4 h of electrolysis, the two peaks at 493.65 and 485.26 eV are attributed to the metallic Sn^0 species.[38] The above results suggest that the co-existence of a small amount of SnS_2 and dominated metallic Sn is crucial for the ECO_2RR as they (Sn/SnS_2) seem to be catalytically active materials.

The evolution of SnS_2-based catalysts during the ECO_2RR was investigated using *in situ* Raman spectroscopy. As depicted in Fig. 4a, the band observed at 315 cm^{-1} corresponds to the A_{1g} mode of SnS_2.[39] For both SnS_2 + PVDF and SnS_2 electrodes, intensities of A_{1g} mode grow weak with the decrease of the applied potential. However, with PVDF introduction, this weakening occurs at a slower rate, which may be due to its hydrophobic nature. In the ATR-SEIRAS spectra (Fig. 4c and d), a broad peak observed between 3000 and 3700 cm^{-1} is attributed to the O–H stretching vibrations (ν_{O-H}),[40] while the peak at 1650 cm^{-1} corresponds to the O–H bending vibrations (δ_{O-H}).[41] Additionally, the peak at 1520 cm^{-1} is associated with carbonate ions (CO_3^{2-}), and the peak at 1370 cm^{-1} is linked to

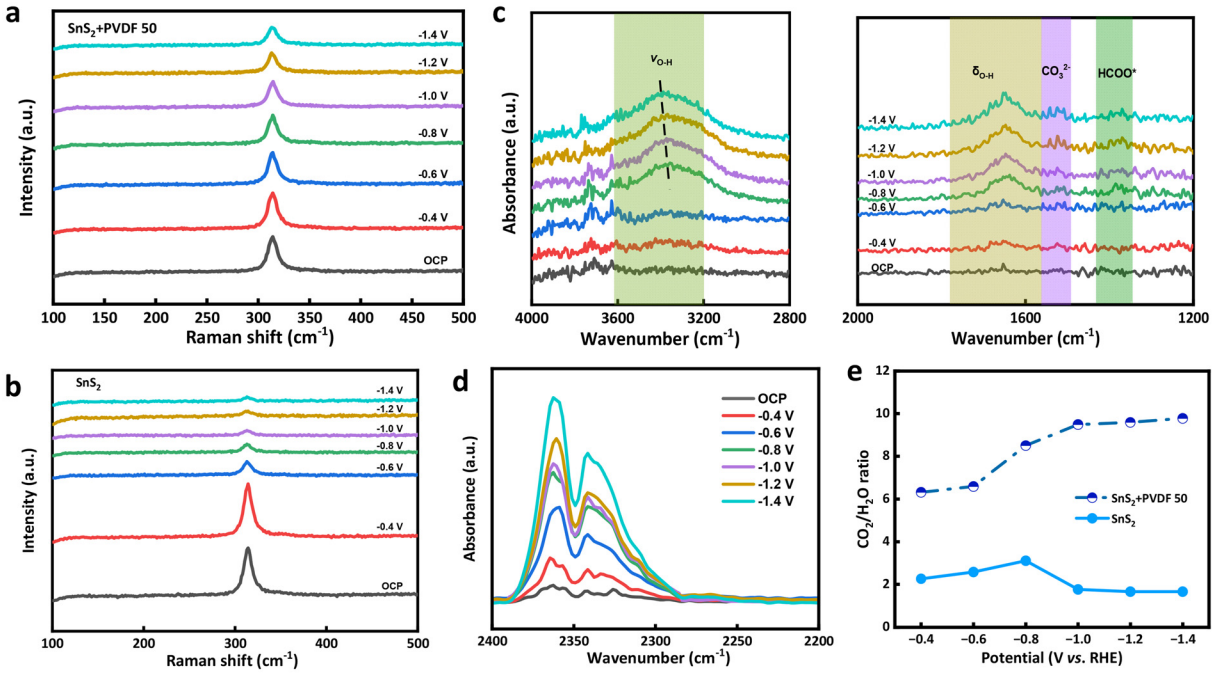

Fig. 4 The *in situ* Raman spectra of (a) SnS_2 + PVDF 50 and (b) SnS_2 with different applied potentials. The *in situ* ATR-SEIRAS spectra of SnS_2 + PVDF 50 in a range of different wavelength segments (c) 4000–3000 cm^{-1} and 2000–1200 cm^{-1}, and (d) 2200–2400 cm^{-1}. (e) CO_2/H_2O ratio of SnS_2 + PVDF 50 and SnS_2 at different applied potentials.

HCOO*.[42] Two distinct peaks located at 2365 and 2340 cm^{-1} are attributed to gaseous CO_2.[43] As illustrated by the ATR-SEIRAS spectra for SnS_2 + PVDF 50, an increase of the ν_{O-H} peak intensity coupled with a blue shift is noted at more negative applied potentials. This indicates a significant decrease in isolated water molecules. In contrast, the ν_{O-H} of the SnS_2 spectra shows only a modest increase along with a red shift (Fig. S18a†). This behavior may be assigned to the enhanced hydrogen bonding interactions resulting from hydrolysis that occurs at the electrified interface,[44] which is consistent with the intensification of the HER. Thus, it is obvious that the SnS_2 + PVDF 50 electrode creates a hydrophobic microenvironment at the gas–liquid–solid interface. In addition, to elucidate how interfacial concentrations of CO_2 and H_2O influence both reaction pathways and selectivity towards HCOOH, *in situ* ATR-SEIRAS was employed. As shown in Fig. 4d, the CO_2 absorption peak of the SnS_2 + PVDF 50 electrode gradually increases as the applied potential becomes more negative. In contrast, the CO_2 absorption peak of SnS_2 reaches the maximum at −0.8 V and subsequently decreases as the applied potential continues to become more negative (Fig. S18b†). Then, by comparing the ratio of CO_2 to H_2O over the SnS_2 + PVDF 50 and SnS_2 electrodes (Fig. S19†), a higher value is observed for SnS_2 + PVDF 50 across −0.4 V to −1.4 V (Fig. 4e). This indicates that the incorporation of hydrophobic PVDF results in higher concentrations of CO_2 around the electrode.[45] Simultaneously, an HCOO* peak appears at −0.8 V for SnS_2 + PVDF 50, which proves the formation of formate. However, there is nearly no change observed for SnS_2 itself. Above all, the *in situ* ATR-SEIRAS analysis reveals that the SnS_2 + PVDF 50 electrode creates a hydrophobic microenvironment, which enhances the ratio of CO_2 to H_2O across three-phase interfaces, and the ECO_2RR performance gets boosted as a consequence. Moreover, the δ_{O-H} peak (1650 cm^{-1}) for SnS_2 + PVDF 50 exhibits an increasing trend due to the reorientation and adsorption of water that is oriented downwards on the electrode surface to facilitate coupling with CO_2 reduction.[46]

Based on the aforementioned analysis, in the three-phase set-up (gas–liquid–solid interface), an effective CO_2RR-to-

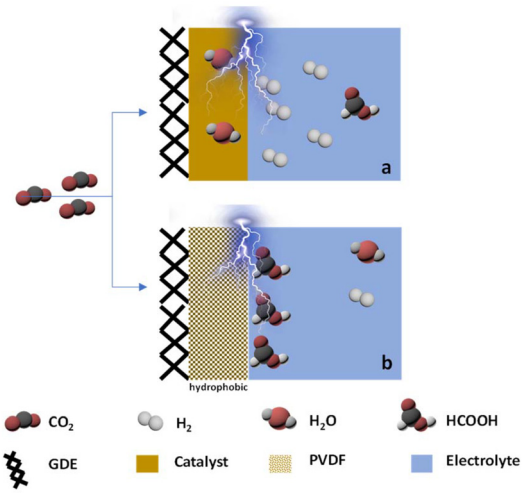

Fig. 5 Illustration of the gas–liquid–solid boundaries before and after modification of the SnS_2 catalyst with PVDF particles.

formate system is generated due to the combination of the SnS_2 catalyst and hydrophobic PVDF particles (Fig. 5). The integration of the hydrophobic polymer and modified SnS_2 catalyst creates a hydrophobic microenvironment that enhances the local ratio of CO_2 to H_2O and constructs more three-phase (solid–liquid–gas) boundaries. The enhanced CO_2 concentration could promote the CO_2 mass transfer, thus hindering the HER and promoting the CO_2 conversion.

Conclusions

In summary, a simple method has been adapted to decorate SnS_2 with polymer PVDF to achieve the pH-universal ECO_2RR to obtain formic acid. The PVDF-modified SnS_2 exhibits a higher formate FE of 98% in 1 M KOH than pure SnS_2. Furthermore, the SnS_2 + PVDF 50 electrode offers excellent stability (>30 h) in 1 M KOH under a current density of 150 mA cm^{-2} with a negligible decrease in FE, yielding a 2.67 mol L^{-1} formate solution. SnS_2 + PVDF 50 could achieve 93% HCOOH FE in 0.05 M H_2SO_4 + 0.5 M K_2SO_4. In particular, its SPCE could reach 72.77% in acidic electrolyte, which is twice more than that under alkaline conditions. The introduction of the hydrophobic polymer PVDF could enhance the local ratio of CO_2/H_2O and generate rich gas–liquid–solid interfaces, as studied using *in situ* ATR-SEIRAS spectra. Furthermore, the increased local ratio of CO_2/H_2O could boost the accessibility of CO_2 to the catalyst surface, thus improving the catalytic activity and inhibiting the HER. *In situ* Raman spectra, post-reaction structure analysis, and performance evaluation point out that SnS_2 undergoes reconstruction to form catalytically active Sn/SnS_2 composites during the ECO_2RR. This work presents a facial and green method to achieve efficient CO_2 conversion to formic acid using a pH-universal catalyst.

Experimental

Materials

Tin(IV) chloride pentahydrate (Adamas-beta, $SnCl_4{\cdot}5H_2O$, 98%, AR), thioacetamide (Macklin C_2H_5NS, 99%, AR), ethanol (DM, CH_3CH_2OH, 99.5% AR), polyvinylidene fluoride (Aladdin, $(CH_2CF_2)_n$), polyvinylpyrrolidone K30 (OKA, $(C_6H_9NO)_n$), potassium bicarbonate (Aladdin, $KHCO_3$, 99.7%, AR), potassium hydroxide (Aladdin, KOH, AR), Nafion perfluorinated resin (Adamas, 5 wt% in the mixture of lower aliphatic alcohols and water, contains 45% water), formic acid solution (Aladdin, HCOOH, 1% w/v), and sulfuric acid (H_2SO_4, 96%, AR) were used without further purification. Ultrapure Millipore water (18.25 MΩ) was used in all experiments. An Ag/AgCl electrode (GaossUnion, R1038), a GDE (SGL, 28 BC), an anion-exchange membrane (DM, Sustanion X37–50), a proton exchange membrane (DuPont, Nafion 117), and Nickel foam (Youveim®) were used.

Synthesis of SnS_2

SnS_2 nanoflowers were synthesized using a modified method based on a previous report.[28] 211.2 mg of $SnCl_4{\cdot}5H_2O$ and 135.2 mg of CH_4N_2S were dissolved in 25 mL of ethanol and then poured into a 50 mL Teflon-lined stainless-steel autoclave. The autoclave was sealed properly and heated at 150 °C for 12 h. After the reaction, the resulting sample was collected by centrifugation at 9500 rpm. The collected sample was washed with ethanol and then dried under vacuum at 70 °C overnight to obtain SnS_2 nanoflowers.

Electrode preparation

4 mg of SnS_2 powder and 1 mg of carbon black (XC-72) were dispersed in 720 μL of isopropanol, 240 μL of ultrapure water, and 40 μL of 5% Nafion to form the SnS_2 ink. A total of 200 μL of the prepared SnS_2 catalyst slurry was dropped onto carbon paper to prepare the SnS_2 electrode with an appropriate catalyst loading (1 mg cm^{-2}). The prepared SnS_2 ink was uniformly mixed using ultrasonication for 1 h. Meanwhile, 5 mg of PVDF was dispersed in 500 μL of DMF and mixed evenly with ultrasonication for 1 h. Next, the two mixtures were mixed and ultrasonicated for an additional hour. Subsequently, 300 μL of the prepared catalyst slurry was dropped onto carbon paper to create the SnS_2 + PVDF 50 electrode. The loading amounts of SnS_2 and PVDF were both 1 mg cm^{-2}. Similarly, SnS_2 + PVDF electrodes with varying mass ratios (10, 20, 30, 40, 60, and 70) were prepared by adjusting the amount of PVDF (0.55 mg, 1.25 mg, 2.14 mg, 3.33 mg, 5 mg, 7.5 mg, and 11.67 mg) in DMF. For the SnS_2 + PVP electrode, 5 mg of PVP was directly added to the as-prepared SnS_2 ink, followed by 1 hour of ultrasonication. Then, 200 μL of the prepared catalyst slurry was dropped onto carbon paper to fabricate the SnS_2 + PVP electrode. The loading amounts of SnS_2 and PVP were both 1 mg cm^{-2}.

Characterization

XRD patterns of catalysts loaded on CP were analyzed using an X-ray diffractometer (Japan Rigaku), operating at 4° min^{-1} over a range of 10°–90°. Morphological features were observed using a TESCAN MIRA3 LMH Field Emission Scanning Electron Microscope, which was operated at 10 kV. The XPS spectra were obtained using a Thermo Scientific ESCALAB 250Xi spectrometer, with measurements conducted *via* a Kratos Analytical AXIS Supra spectrometer utilizing Al Kα radiation. The binding energy scale was calibrated using the C 1s peak, fixed at 284.8 eV. Water contact angle measurements were performed using a contact angle goniometer from KRUSS (Germany).

Electrochemical measurements

The ECO_2RR was conducted in a typical flow cell system using circulating electrolytes: alkaline (1 M KOH), neutral (0.5 M $KHCO_3$), and acidic (0.05 M H_2SO_4 + 0.5 M K_2SO_4). The CO_2RR electrolysis was performed using a CHI 760e electrochemical workstation. The prepared SnS_2 + PVDF 50, SnS_2 + PVP, and

SnS_2 electrodes were used as the working electrodes. An Ag/AgCl electrode with a saturated 3 M KCl solution served as the reference electrode. Foamed nickel was employed as the counter electrode in alkaline and neutral electrolytes, while IrO_2 supported on Ti mesh was used as the counter electrode in the acidic electrolyte. In the ECO_2RR process in alkaline and neutral electrolytes, both the anolyte and catholyte consisted of 30 mL of either 1 M KOH or 0.5 M $KHCO_3$ respectively. An anion-exchange membrane (Sustanion) was employed to separate the anodic and cathodic compartments. For processes employing acidic catholytes, both the anolyte and catholyte comprised 30 mL of electrolytes (0.05 M H_2SO_4 + 0.5 M K_2SO_4), with a Nafion-N117 membrane utilized to divide the anodic and cathodic compartments. The catholyte was circulated through a peristaltic pump at a flow rate of 5 mL min^{-1}, while the anolyte was cycled through a gas–liquid mixed flow pump. CO_2 gas was delivered past the GDLs of the cathode at a flow rate of 15 sccm. The inlet gas flow rate was measured using a mass flow meter (HPI S4933/MT), and the outlet gas flow rate was recorded with a mass flow meter (Sevenstar D07). All measured potentials were converted to values relative to the RHE using the following equation, without IR compensation.

$$E_{(\text{V } vs.\ \text{RHE})} = E_{(\text{V } vs.\ \text{Ag/AgCl})} + 0.0591 \times \text{pH} + 0.197(\text{V}) \quad (1)$$

EIS tests were conducted at open circuit potential with an amplitude of 5 mV over a frequency range from 0.01 Hz to 100 kHz in 0.5 M $KHCO_3$. LSV scanning was conducted at a scan rate of 10 mV s^{-1}. C_{dl} was determined through various CV measurements across different scan rates in 0.5 M $KHCO_3$: specifically at intervals of 20, 40, 60, 80, and 100 mV s^{-1}.

Electrocatalytic CO_2RR product analysis

Gas products were analyzed by GC using an Agilent 8890 GC system. H_2 was detected using thermal conductivity detectors (TCD), while CO was detected using a flame ionization detector (FID). The FE of the gas products was calculated as follows:

$$\text{FE}_{\text{gas}}(\%) = Q_{\text{gas}}/Q_{\text{total}} = N \times \text{F} \times n_{\text{gas}}/Q \quad (2)$$

where F represents the faradaic constant, N denotes the number of electrons transferred from CO_2 to the products, n_{gas} indicates the total amount of gas products (in moles), and Q signifies the total charge (in coulombs). Liquid products were analyzed using a HPLC system equipped with diode-array detectors (DAD). An H_2SO_4 solution with a pH of 2.5 was utilized as the mobile phase, and areas with varying concentrations of HCOOH solution (200–4000 ppm) were employed to quantify the concentration of liquid products. The FE of the gas products was calculated as follows:

$$\text{FE}_{\text{HCOOH}}(\%) = Q_{\text{liquid}}/Q_{\text{total}} = n_{\text{liquid}} \times N \times \text{F}/Q \times 100\% \quad (3)$$

where n_{liquid} is the amount of liquid products produced within a specific time (t) frame, v is the flow rate of CO_2 and t is the duration of the electrolysis process. The SPCE was calculated as follows,

$$\text{SPCE} = n_{\text{liquid}}/(v \times t/24.5) \quad (4)$$

where n_{liquid} is the amount of liquid products within a certain time (t) frame, v is the flow rate of CO_2, and t is defined as above.

In situ ATR-SEIRAS

In situ ATR-SEIRAS was conducted using a Bruker Tensor 27 ATR-FTIR Spectrometer equipped with a liquid nitrogen-cooled MCT detector and an electrochemistry *in situ* ATR infrared reaction cell (EC-ATR-H) from Beijing Scistar Technology Co., Ltd. An Au electrode with coated catalysts was installed on top of a silicon crystal and served as the working electrode. A Pt wire and an Ag/AgCl electrode were employed as the counter and reference electrodes, respectively. The detector was cooled with liquid nitrogen for at least 30 minutes before detection to ensure signal stability. The electrolyte (0.5 M $KHCO_3$) was purged with CO_2 for no less than 30 minutes to achieve saturation before testing and continued to be purged with CO_2 throughout the experiment. All spectra were collected by incrementally varying the potential from −0.4 V to −1.4 V, while the spectrum obtained at an open circuit voltage served as the baseline for initial comparison.

In situ Raman spectroscopy

In situ Raman spectroscopy was conducted utilizing a Renishaw inVia Reflex micro-Raman spectrometer that employed a 532 nm laser as its excitation source. Before testing, the electrolyte (0.5 M $KHCO_3$) underwent CO_2 purging for at least 30 minutes; subsequently, this saturated electrolyte was used for further analysis. During *in situ* Raman testing, all spectra were sequentially collected by adjusting the potential from −0.4 V to −1.4 V.

Abbreviations

Nomenclature

ATR-SEIRAS	Attenuated total reflectance surface-enhanced infrared absorption spectroscopy
C_{dl}	Double-layer capacitance
CP	Carbon paper
CV	Cyclic voltammetry
DAD	Diode-array detector
DMF	Dimethyl formamide
ECSA	Electrochemical active surface area
ECO_2RR	Electrocatalytic CO_2 reduction reaction
EIS	Electrochemical impedance spectroscopy
FE	Faradaic efficiency
FID	Flame ionization detector
GC	Gas chromatography
GDE	Gas-diffusion electrode
HER	Hydrogen evolution reaction
HPLC	High-performance liquid chromatography
LSV	Linear sweep voltammetry
PVDF	Polyvinylidene fluoride

PVP	Polyvinyl pyrrolidone
R_{ct}	Charge transfer resistance
RHE	Reversible hydrogen electrode
SEM	Scanning electron microscopy
SPCE	Single-pass carbon efficiency
TCD	Thermal conductivity detector
XPS	X-ray photoelectron spectroscopy
XRD	X-ray powder diffraction

Italics

E	Applied potential (V)
f	The frequency of EIS tests (Hz)
N	Transferred electrons from CO_2 to products
n_{gas}	Total amount of gas products (mol)
n_{liquid}	Total amount of liquid products (mol)
Q	The amount of total charge (C)
R	faradaic constant (C mol^{-1})
t	Reaction time (s)
T	Temperature (°C)
v	The flow rate of inlet and outlet gas (sccm)

Author contributions

Z. W. Dong: data curation, investigation, formal analysis, and writing – original draft; Z. Y. Wang: validation; Y. L. Jia: conceptualization and writing – review & editing; A. Rajendran: supervision and writing – review & editing; W.-Y. Li: funding acquisition, methodology, resources, supervision, and writing – review & editing.

Data availability

The data supporting this article have been included as part of the ESI.†

Conflicts of interest

The authors declare that they have no known competing financial interests or personal relationships that could have appeared to influence the work reported in this paper.

Acknowledgements

This work was financially supported by the National Key Research and Development Program of China (2022YFE0208400), the Fundamental Research Project of Shanxi Province (202303021212031), and the Fundamental Research Funds for the Central Universities (2022ZFJH004).

References

1 J. H. Montoya, L. C. Seitz, P. Chakthranont, A. Vojvodic, T. F. Jaramillo and J. K. Nørskov, *Nat. Mater.*, 2017, **16**, 70–81.
2 M. Filonchyk, M. P. Peterson, L. Zhang, V. Hurynovich and Y. He, *Sci. Total Environ.*, 2024, **935**, 173359.
3 U. A. Bhatti, M. A. Bhatti, H. Tang, M. S. Syam, E. M. Awwad, M. Sharaf and Y. Y. Ghadi, *Environ. Res.*, 2024, **245**, 118049.
4 Y. Wang, J. Zhang, J. Zhao, Y. Wei, S. Chen, H. Zhao, Y. Su, S. Ding and C. Xiao, *ACS Catal.*, 2024, **14**, 3457–3465.
5 M. Fang, M. Wang, Z. Wang, Z. Zhang, H. Zhou, L. Dai, Y. Zhu and L. Jiang, *J. Am. Chem. Soc.*, 2023, **145**, 11323–11332.
6 Q. Gong, P. Ding, M. Xu, X. Zhu, M. Wang, J. Deng, Q. Ma, N. Han, Y. Zhu, J. Lu, Z. Feng, Y. Li, W. Zhou and Y. Li, *Nat. Commun.*, 2019, **10**, 2807.
7 M. Pérez-Fortes, J. C. Schöneberger, A. Boulamanti, G. Harrison and E. Tzimas, *Int. J. Hydrogen Energy*, 2016, **41**, 16444–16462.
8 J. T. Feaster, C. Shi, E. R. Cave, T. Hatsukade, D. N. Abram, K. P. Kuhl, C. Hahn, J. K. Nørskov and T. F. Jaramillo, *ACS Catal.*, 2017, **7**, 4822–4827.
9 Y. Kamakura, C. Suppaso, I. Yamamoto, R. Mizuochi, Y. Asai, T. Motohashi, D. Tanaka and K. Maeda, *Angew. Chem., Int. Ed.*, 2023, **62**, e202305923.
10 Y. Yao, W. Zhuang, R. Li, K. Dong, Y. Luo, X. He, S. Sun, S. Alfaifi, X. Sun and W. Hu, *Chem. Commun.*, 2023, **59**, 9017–9028.
11 L.-C. Weng, A. T. Bell and A. Z. Weber, *Phys. Chem. Chem. Phys.*, 2018, **20**, 16973–16984.
12 M. E. Leonard, L. E. Clarke, A. Forner-Cuenca, S. M. Brown and F. R. Brushett, *ChemSusChem*, 2020, **13**, 400–411.
13 R. Kas, K. Yang, D. Bohra, R. Kortlever, T. Burdyny and W. A. Smith, *Chem. Sci.*, 2020, **11**, 1738–1749.
14 Y. Chen, Y. Zhang, Z. Li, M. Liu, Q. Wu, T. W. B. Lo, Z. Hu and L. Y. S. Lee, *ACS Nano*, 2024, **18**, 19345–19353.
15 Z. Xing, L. Hu, D. S. Ripatti, X. Hu and X. Feng, *Nat. Commun.*, 2021, **12**, 136.
16 Z. Xing, X. Hu and X. Feng, *ACS Energy Lett.*, 2021, **6**, 1694–1702.
17 S. Wang, Z. Wu, C. Xu, S. Jiang, H.-Q. Peng, W. Zhang, B. Liu and Y.-F. Song, *ACS Appl. Mater. Interfaces*, 2022, **14**, 45423–45432.
18 J. Chen, H. Qiu, Y. Zhao, H. Yang, L. Fan, Z. Liu, S. Xi, G. Zheng, J. Chen, L. Chen, Y. Liu, L. Guo and L. Wang, *Nat. Commun.*, 2024, **15**, 5893.
19 W. Li, C. Yu, X. Tan, Y. Ren, Y. Zhang, S. Cui, Y. Yang and J. Qiu, *ACS Catal.*, 2024, **14**, 8050–8061.
20 Y. Yao, E. P. Delmo and M. Shao, *Angew. Chem., Int. Ed.*, 2025, **64**, e202415894.
21 L. Zhang, J. Feng, S. Liu, X. Tan, L. Wu, S. Jia, L. Xu, X. Ma, X. Song, J. Ma, X. Sun and B. Han, *Adv. Mater.*, 2023, **35**, 2209590.
22 Z. Wang, Y. Li, X. Zhao, S. Chen, Q. Nian, X. Luo, J. Fan, D. Ruan, B.-Q. Xiong and X. Ren, *J. Am. Chem. Soc.*, 2023, **145**, 6339–6348.
23 M. H. Hicks, W. Nie, A. E. Boehme, H. A. Atwater, T. Agapie and J. C. Peters, *J. Am. Chem. Soc.*, 2024, **146**, 25282–25289.

24 J. Gu, S. Liu, W. Ni, W. Ren, S. Haussener and X. Hu, *Nat. Catal.*, 2022, **5**, 268–276.
25 J. E. Huang, F. Li, A. Ozden, A. S. Rasouli, F. P. G. de Arquer, S. Liu, S. Zhang, M. Luo, X. Wang, Y. Lum, Y. Xu, K. Bertens, R. K. Miao, C.-T. Dinh, D. Sinton and E. H. Sargent, *Science*, 2021, **372**, 1074–1078.
26 Q. Wu, D. H. Si, J. Liang, Y. B. Huang and R. Cao, *Appl. Catal., B*, 2023, **333**, 122803.
27 M. Wang, L. Lin, Z. Zheng, Z. Jiao, W. Hua, G. Wang, X. Ke, Y. Lian, F. Lyu, J. Zhong, Z. Deng and Y. Peng, *Energy Environ. Sci.*, 2023, **16**, 4423–4431.
28 M. Chen, S. Wan, L. Zhong, D. Liu, H. Yang, C. Li, Z. Huang, C. Liu, J. Chen, H. Pan, D.-S. Li, S. Li, Q. Yan and B. Liu, *Angew. Chem., Int. Ed.*, 2021, **60**, 26233–26237.
29 Q. Chen, H. Zhu, Z. Guo, Z. Yan, G. Yang, Y. Zheng, Y. Xing, H. Yin and T. Wu, *J. Alloys Compd.*, 2024, **991**, 174475.
30 M. Pakan, M. Mirabi and A. Valipour, *Chemosphere*, 2023, **337**, 139333.
31 H.-Q. Liang, S. Zhao, X.-M. Hu, M. Ceccato, T. Skrydstrup and K. Daasbjerg, *ACS Catal.*, 2021, **11**, 958–966.
32 J. Xian, Q. Hua, Z. Jiang, Y. Ma and W. Huang, *Langmuir*, 2012, **28**, 6736–6741.
33 T. H. M. Pham, J. Zhang, M. Li, T.-H. Shen, Y. Ko, V. Tileli, W. Luo and A. Züttel, *Adv. Energy Mater.*, 2022, **12**, 2103663.
34 H. Liu, Y. Su, Z. Liu, H. Chuai, S. Zhang and X. Ma, *Nano Energy*, 2023, **105**, 108031.
35 L. Lin, X. He, X.-G. Zhang, W. Ma, B. Zhang, D. Wei, S. Xie, Q. Zhang, X. Yi and Y. Wang, *Angew. Chem., Int. Ed.*, 2023, **62**, e202214959.
36 P. Waszczuk, P. Zelenay and J. Sobkowski, *Electrochim. Acta*, 1995, **40**, 1717–1721.
37 A. R. Woldu, P. Talebi, A. G. Yohannes, J. Xu, X.-D. Wu, S. Siahrostami, L. Hu and X.-C. Huang, *Angew. Chem., Int. Ed.*, 2023, **62**, e202301621.
38 F. Li, L. Chen, M. Xue, T. Williams, Y. Zhang, D. R. MacFarlane and J. Zhang, *Nano Energy*, 2017, **31**, 270–277.
39 J. Feng, J. Fan, Z. Zhang, Y. Gao, S. Xue, G. Cai and J. S. Zhao, *Adv. Funct. Mater.*, 2024, **34**, 2401228.
40 X. Tong, P. Zhang, P. Chen, Z. He, X. Kang, Y. Yin, Y. Cheng, M. Zhou, L. Jing, C. Wang, B. Xu, L. Zheng, X. Xing, Z. Wu and B. Han, *Angew. Chem., Int. Ed.*, 2025, **64**, e202413005.
41 Z.-Z. Wu, X.-L. Zhang, Z.-Z. Niu, F.-Y. Gao, P.-P. Yang, L.-P. Chi, L. Shi, W.-S. Wei, R. Liu, Z. Chen, S. Hu, X. Zheng and M.-R. Gao, *J. Am. Chem. Soc.*, 2022, **144**, 259–269.
42 T. Dong, H. Li, Z. Wang, Y. Geng, R. Chang, X. Tian, J. Lai, S. Feng and L. Wang, *Nano Res.*, 2024, **17**, 5817–5825.
43 R. Zhao, H. Luo, T. Ouyang and Z.-Q. Liu, *ACS Nano*, 2024, **18**, 35749–35757.
44 Z.-Q. Zhang, S. Banerjee, V. S. Thoi and A. S. Hall, *J. Phys. Chem. Lett.*, 2020, **11**, 5457–5463.
45 Z. Xu, X. Zhang and Q. Wang, *Chem. Eng. J.*, 2024, **492**, 152164.
46 Q. Luo, H. Duan, M. C. McLaughlin, K. Wei, J. Tapia, J. A. Adewuyi, S. Shuster, M. Liaqat, S. L. Suib, G. Ung, P. Bai, S. Sun and J. He, *Chem. Sci.*, 2023, **14**, 9664–9677.

